Frequency Stabilization Method for Grid Integration of Large-scale Centralized Wind Farms via VSC-HVDC Technology

Yanjian Peng*, Yong Li*, Fang Liu†, Zhiwei Xu**, and Yijia Cao*

*College of Electrical and Information Engineering, Hunan University, Changsha, China
†School of Information Science and Engineering, Central South University, Changsha, China
**Hunan Provincial Key Laboratory of Wind Generator and Its Control, Hunan Institute of Engineering, Xiangtan, China

Abstract

This work proposes a control method of frequency stabilization for grid integration of large-scale wind farms via the voltage source converter-based high-voltage direct current (VSC-HVDC) technology. First, the topology of grid integration of a large-scale wind farm via the VSC-HVDC link is provided, and simple control strategies for wind turbines, wind farm side VSC (WFVSC), and grid side VSC are presented. Second, a mathematical model between the phase angle of WFVSC and the frequency of the wind farm is established. The control principle of the large-scale wind power integrated system is analyzed in theory in accordance with the mathematical model. Third, frequency and AC voltage controllers of WFVSC are designed based on the mathematical model of the relationships between the phase angle of WFVSC and the frequency of the wind farm, and between the modulation index of WFVSC and the voltage of the wind farm. Corresponding controller structures are established by deriving a transfer function, and an optimization method for selecting the parameters of the frequency controller is presented. Finally, a case study is performed under different operating conditions by using the DIgSILENT/PowerFactory software. Results show that the proposed control method has good performance in the frequency stabilization of the large-scale wind power integrated system via the VSC-HVDC technology.

Key words: Frequency stabilization, Large-scale wind farm, Phase angle, Voltage source converter-based high voltage direct current (VSC-HVDC)

I. INTRODUCTION

Renewable energy, especially wind power, is widely applied worldwide due to environmental considerations [1], [2]. Many large-scale onshore and offshore wind farms have been put into operation or are under construction in China, United States, India, United Kingdom, Netherlands, Denmark, Germany, and other countries [3]. The increasing penetration of wind power and the growing size of wind farms will bring some technical challenges to power systems due to the variability and uncertainty of wind speed that involve frequency and voltage disturbances [4]-[6]. These problems affect the safety and stability of wind farms or power systems.

Many large-scale wind farms are far from load centers. Therefore, an efficient way to transmit wind power from large-scale wind farms to load centers is necessary. High-voltage alternating current (HVAC) transmission technology is often used for remote large-scale wind farms due to its low cost. However, as the transmission distance increases, HVAC cables have relatively high capacitance, which produces charging current in the HVAC cables. This situation results in significant losses in HVAC cables and reduced transmission efficiency [7]-[9]. Therefore, it is not practical to use the HVAC cables to transmit large amounts of power over distances greater than 50–75 km [10].

Owing to the development of power electronic devices, high-voltage direct current (HVDC) transmission technology is regarded as an effective way to connect large-scale wind farms to load centers and transmit wind power from these farms because DC transmission systems offer attractive solutions to power transfer over long distances [11], [12].

Moreover, the power losses of HVDC transmission systems are smaller than those of HVAC transmission systems because the former is unaffected by charging current, which exists in HVAC cables. Thus, the efficiency of HVDC transmission is higher than that of HVAC transmission when the transmission distance between large-scale wind farms and load centers is large.

HVDC links are of two types. One is the line-commutated converter (LCC) type, which is also called the current source converter (CSC) type, that uses thyristors [13], [14]; the other is the force-commutated voltage source converter type that uses full-controllable power electronic devices [15], such as gate turn-off thyristors (GTO) and insulated gate bipolar transistors (IGBT). A number of studies have integrated remote large-scale wind farms through LCC-HVDC technology [16]–[18]. With the transmission power capacity increase, LCC-HVDC converters need to absorb large amounts of reactive power, so it need to configure large-capacity reactive power compensation devices, such as capacitors and filter banks [13], [16], static VAR compensators (SVC) [17], and static synchronous compensators (STATCOM) [18], for reactive power and voltage support. In other words, LCC-HVDC technology requires a large station space for its converter and reactive compensator. However, having a large space in a large-scale offshore wind farm is uneconomical. LCC-HVDC technology has also other drawbacks, such as non-independent control of active and reactive power, large amount of harmonics, and lack of black start-up capability, and these drawbacks limit the application of LCC-HVDC technology [19].

VSC-HVDC technology presents several advantages over LCC-HVDC technology. For example, the installation space for a VSC-HVDC converter station is smaller than that for LCC-HVDC. VSC-HVDC technology has an inherent capability to control independent active and reactive power by using the VSC converter station. Moreover, VSC-HVDC can change the power flow direction without reversing the voltage polarity of DC cables [20]. The most important advantage of VSC-HVDC technology is that it does not require external voltage sources during its operation, and this advantage makes VSC-HVDC technology more suitable than LCC-HVDC technology for connecting remote large-scale wind farms (extremely offshore) with weak grids [21]. This work focuses on the integration of a large-scale wind farm through VSC-HVDC technology.

Large-scale wind farms that are grid-connected via an HVDC link can also bring some technical challenges to power system operators. For example, if imbalance exists between the total active power generated by all wind turbines and the power transferred to the HVDC link, then the frequency of the wind farm side may vary [22]. A frequency control method was proposed in [22], [23], and [24] to regulate the rectifier firing angle or DC-link current of an LCC-HVDC link, and the power flow was controlled correspondingly. However, this control method is inapplicable to the integration of large-scale wind farms via VSC-HVDC technology. Meanwhile, the participation of wind turbines in system frequency regulation was investigated in [2] and [5]. A drawback of these methods is long latency period because control commands (e.g., frequency commands) are sent to each wind turbine through a standard supervisory control and data acquisition (SCADA) system. Moreover, these studies did not consider the frequency regulation capability of VSC-HVDC.

The frequency support capability of wind turbines and a VSC-HVDC converter were combined in [25] to improve the system frequency response. However, the coordinated frequency control strategy proposed in [25] may cause wind turbines to work in non-optimal conditions. For example, if the power generated by wind turbines cannot be fully transmitted to the grid, power reduction control will be implemented in the wind turbines; this condition may not be suitable for large-scale wind farms [26]. Moreover, different wind turbine types, such as doubly fed induction generators (DFIG) [21]-[24], [26] and permanent magnet synchronous generators (PMSG) [20], [25], have been investigated in previous studies. DFIG is discussed in this work.

Different from traditional frequency control strategies for the wind-farm-side VSC (WFVSC) of VSC-HVDC links, this work further investigates the control concept in [23] and combines it with frequency control of large-scale wind farm integration via VSC-HVDC technology. The frequency support capability of the WFVSC of the VSC-HVDC link is fully utilized to regulate the frequency of the large-scale wind farm side. The relationship between the frequency deviation of the wind farm side and phase angle of WFVSC is represented by a detailed mathematical model in the design of the frequency controller. The power flow can be regulated by controlling the phase angle of WFVSC. The active power generated by wind farms is transmitted to the VSC-HVDC link efficiently even when such power fluctuates within a wide range. Therefore, active balance between the large-scale wind farm and VSC-HVDC link is achieved, which means that there is no or few frequency deviation in the large-scale wind farm side.

The rest of this work is organized as follows. Section II presents the topology of a large-scale wind farm and VSC-HVDC transmission system. Control strategies of DFIG, WFVSC, and grid-side VSC (GSVSC) are described, and a mathematical model of the relationship between the phase angle of WFVSC and frequency of a large-scale wind farm is established. A frequency controller is designed according to the corresponding mathematical model. Section III presents an optimized method for selecting control parameters. A case study is provided in Section IV, and the conclusion is presented in Section V.

II. System Topology and Frequency Control

Fig. 1 shows a single-line diagram of a large-scale wind farm and VSC-HVDC transmission system. The transmission system mainly consists of a DFIG-based large-scale wind farm, WFVSC, and GSVSC.

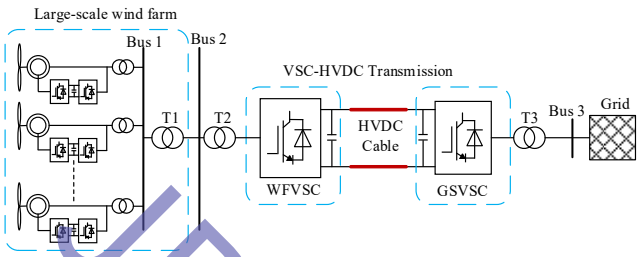

Fig. 1. Single-line diagram of a large-scale wind farm and VSC-HVDC transmission system.

The large-scale wind farm comprises 300 DFIGs, and the rating of each DFIG is 2.0 MVA. Therefore, the total capacity of the large-scale wind farm is 600 MVA. The models of DFIG and its control strategy have already been introduced in [21] and are no longer discussed here. The rated voltage of bus 2 is 400 kV, and the rated capacity of WFVSC and GSVSC is 1216 MVA. The detailed parameters of the VSC-HVDC transmission system are given in Table II of the Appendix.

A. Operation Characteristic of DFIG

The mechanical power of DFIG can be expressed as [27]

$$P_{mec} = \frac{1}{2}\rho\pi R^2 C_p(\lambda,\beta)v^3, \quad (1)$$

where ρ is air density, R is the radius of the turbine, v is wind speed, and C_p (λ, β) is the power coefficient, which is influenced by the value of pitch angle β and tip speed ratio λ.

$$\lambda = \frac{\omega_{opt} R}{v}, \quad (2)$$

$$\lambda_i = \frac{1}{\frac{1}{\lambda + 0.08\beta} - \frac{0.035}{1+\beta^3}}, \quad (3)$$

$$C_p(\lambda,\beta) = 0.5176\left(\frac{116}{\lambda_i} - 0.4\beta - 5\right)e^{-\frac{21}{\lambda_i}} + 0.0068\lambda, \quad (4)$$

where ω_{opt} is the optimal wind turbine rotational speed. DFIG starts to operate at the cut-in wind speed and stops at the cut-off wind speed. The operation region of DFIG can be divided into four parts according to wind speed [27], and these parts are region I ($v < v_{cut\text{-}in}$), region II ($v_{cut\text{-}in} < v < v_{rated}$), region III ($v_{rated} < v < v_{cut\text{-}off}$), and region IV ($v > v_{cut\text{-}off}$). Fig. 2 shows the four operation regions of a real 2 MW DFIG.

The four operation regions of DFIG are briefly discussed as follows.

(1) Region I: No power originates from DFIG because the wind speed is lower than the cut-in wind speed.

(2) Region II: The wind turbine can track the maximum power point of the mechanical power curves by controlling the value of pitch angle β and power coefficient C_p (λ, β). Specifically, power coefficient C_p (λ, β) is controlled to obtain an optimal value, and pitch angle β is controlled to 0. Therefore, region II is also called the maximum power point tracking region.

(3) Region III: DFIG is operated at the maximum rotor speed, and pitch angle β is not equal to 0 because the wind speed is higher than the rated value. Thus, the DFIG can obtain constant rated power.

(4) Region IV: DFIG is shut down for protection because the wind speed exceeds the cut-off value.

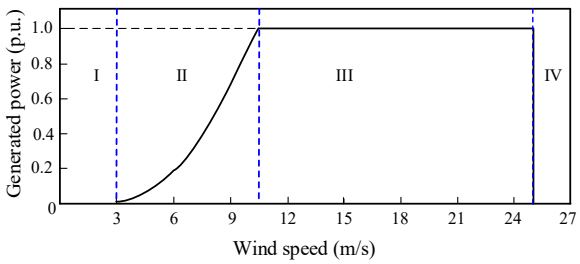

Fig. 2. Power–wind speed curve of a real 2 MW DFIG.

B. Structure of the Frequency Controller

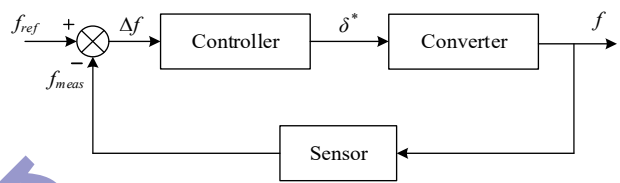

Fig. 3. Structure of the frequency controller.

Fig. 3 shows the structure of the frequency controller applied to WFVSC. The deviation, Δf, between reference frequency f_{ref} and measured frequency f_{meas} in the large-scale wind farm is adjusted by a controller. Thus, we can obtain a phase angle reference value, and the power flow can be regulated by controlling the phase angle. Active power balance exists between the large-scale wind farm and HVDC link Therefore, the frequency of the large-scale wind farm can be kept stable. The structure of the AC voltage controller of WFVSC is similar to that of the frequency controller and is not discussed in this paper anymore.

C. Mathematical Model of the Frequency Controller

The power losses of WFVSC are disregarded in order to simplify the model of large-scale wind farm integration via the VSC-HVDC link, and the DC voltage is kept constant under normal operation. The DC voltage is kept stable by controlling the GSVSC, which uses the constant DC voltage control method. Thus, the DC link and GSVSC can be replaced as a constant DC voltage source [24]. Fig. 4 shows a diagram of WFVSC and the large-scale wind farm, in which an equivalent DFIG, a transformer, a reactor, and a WFVSC are present.

By disregarding the resistance loss and harmonic component

of the reactor, the active power transmitted from the large-scale wind farm to the VSC-HVDC link can be expressed as [28]

$$P_s = \frac{V_{s1}V_1}{X_1}\sin\delta\,, \tag{5}$$

where V_{s1} and V_1 are the AC voltages on the two sides of reactor L_1, respectively, and X_1 is the impedance of the reactor. δ is the phase difference between V_{s1} and V_1 and the phase angle for controlling WFVSC. Eq. (5) shows that the active power flow from the large-scale wind farm to the VSC-HVDC link can be regulated by changing the δ value.

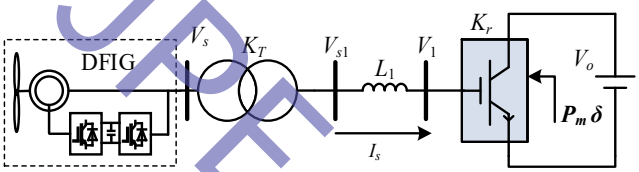

Fig. 4. Diagram of WFVSC and a large-scale wind farm.

The magnetic field, which is formed by the stator and the rotor winding of the induction generator remains stable under steady-state operation. The stator flux is also stable. Thus, $d\psi_s/dt$=0. If the resistance of the stator is ignored, then the voltage of the stator can be described as

$$V_s \approx \omega_1\psi\,, \tag{6}$$

where V_s and ω_1 are the voltage and angular frequency of the stator, respectively.

According to the Kirchhoff's voltage law (KVL) and Fig. 4, the voltage of the reactor can be obtained as

$$V_{L1} = L_1\frac{dI_s}{dt} = V_{s1} - V_1\,, \tag{7}$$

where I_s is the current of reactor L_1. V_1 can be obtained as

$$V_1 = V_{s1} - L_1\frac{dI_s}{dt}\,, \tag{8}$$

The d-q transformation equivalent equation of Eq. (8) can be presented as

$$\begin{cases} V_{1d} = V_{s1d} - L_1\dfrac{dI_{sd}}{dt} + \omega_1 L_1 I_{sq} \\ V_{1q} = V_{s1q} - L_1\dfrac{dI_{sq}}{dt} - \omega_1 L_1 I_{sd} \end{cases}, \tag{9}$$

where V_{1d}, V_{1q}, V_{s1d}, V_{s1q}, I_{sd}, and I_{sq} are the d-q axis components of V_1, V_{s1}, and I_s.

In a steady-state condition, current I_s reaches a constant value, and the derivative of I_s is equal to 0. Therefore, dI_{sd}/dt=0 and dI_{sq}/dt=0. WFVSC uses the voltage-oriented vector control strategy, and the d-axis rotating coordinate system is oriented to stator voltage vector V_s. Thus, the d-q axis components of V_s can be expressed as

$$\begin{cases} V_{sd} = V_s \approx \omega_1 L_0 I_{sm} \\ V_{sq} = 0 \end{cases}, \tag{10}$$

where L_0 and I_{sm} are the excitation inductance and excitation current of DFIG, respectively. The d-q axis components of V_{s1} can be described as

$$\begin{cases} V_{s1d} = V_{s1} \approx K_T\omega_1 L_0 I_{sm} \\ V_{s1q} = 0 \end{cases}, \tag{11}$$

where K_T is the transformer turns ratio.

By combining Eqs. (9) and (11), the following equation can be obtained as

$$\begin{cases} V_{1d} = K_T\omega_1 L_0 I_{sm} + \omega_1 L_1 I_{sq} \\ V_{1q} = -\omega_1 L_1 I_{sd} \end{cases}. \tag{12}$$

The magnitude of V_1 can be expressed as

$$|V_1| = \sqrt{(K_T\omega_1 L_0 I_{sm} + \omega_1 L_1 I_{sq})^2 + (\omega_1 L_1 I_{sd})^2}\,. \tag{13}$$

According to the principle of pulse width modulation (PWM), the relationship between the DC voltage and AC voltage of WFVSC can be obtained as

$$V_0 = K_\gamma P_m V_1 \Leftrightarrow V_1 = \frac{V_0}{K_\gamma P_m}\,, \tag{14}$$

where V_{dc}, K_γ, and P_m are the DC voltage, DC voltage utilization ratio under different PWM trigger modes, and modulation index, respectively. When the system operates in a steady-state condition, DC voltage V_{dc} remains constant; thus, the differential equation that links AC voltage V_1 to modulation index P_m can be expressed as

$$\frac{\partial V_1}{\partial P_m} = -\frac{V_0}{K_\gamma P_m^2}\,. \tag{15}$$

The transfer function between AC voltage V_1 and modulation index P_m of WFVSC can be described as

$$W_0(s) = \frac{V_1(s)}{P_m(s)} = -\frac{V_0}{K_\gamma P_m^2}\,. \tag{16}$$

Due to the d-axis direction of the synchronous rotating coordinate system is oriented to stator voltage vector V_s, the active power of DFIG can be expressed as

$$P = \frac{3}{2}V_{s1d}I_{sd}\,, \tag{17}$$

where V_{sd} and I_{dfd} are the d-axis component of the voltage and current of DFIG, respectively.

Neglecting the resistance losses of the transformer, the power that wind turbines produce is equal to the power that the VSC transmits. Combining Eqs. (5) and (17), the following equation can be obtained as

$$\frac{V_{s1}V_1}{X_1}\sin\delta = \frac{3}{2}V_{s1d}I_{sd}\,. \tag{18}$$

According to Eqs. (11), (13), and (18), the equation that can reflect the relationship between angular frequency ω_1 and phase angle δ is obtained as

$$(K_T\omega_1 L_0 I_{sm} + \omega_1 L_1 I_{sq})^2 + (\omega_1 L_1 I_{sd})^2) - (\frac{3\omega_1 L_1 I_{sd}}{2\sin\delta})^2 = 0\,. \tag{19}$$

During steady-state operations, currents I_{sd}, I_{sq}, and I_{sm} reach their reference value; therefore, they can be replaced by their command values I^*_{sd}, I^*_{sq}, and I^*_{sm}, respectively. The differential

equation that can describe the dynamic characteristic of frequency with respect to variations in phase angle δ can be derived from Eq. (19) as follows:

$$W(s)=\frac{\omega(s)}{\delta(s)}=\frac{K_d I_{sd}^{*\,2}}{(K_T L_0 I_{sm}^{*})^2+(L_1 I_{sd}^{*})^2}, \quad (20)$$

where $K_d=\dfrac{(3X_1)^2\cos\delta}{4\omega_1(\sin\delta)^3}$.

Eqs. (16) and (20) show that the AC voltage and frequency depend on modulation index P_m and phase angle δ, respectively. These two equations are the foundation for designing the control parameters of WFVSC, as mentioned in Section III.

D. Frequency Control Mechanism of WFVSC

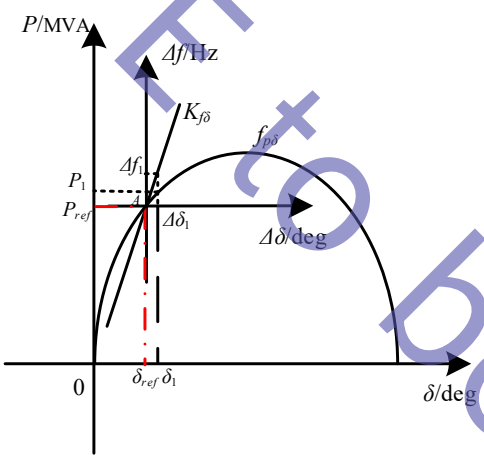

Fig. 5. Frequency control mechanism of WFVSC.

Fig. 5 shows the frequency control mechanism of WFVSC. The δ–P curve represents the relationship between the active power transmitted from the large-scale wind farm and the phase angle of WFVSC. WFVSC is controlled by phase angle δ and modulation index P_m. The detailed control strategy is given in the next chapter. Furthermore, with Eq. (19), the $\Delta\delta$–Δf curve can be obtained, as shown in Fig. 5, which can reflect the relationship between the frequency deviation and phase angle deviation of WFVSC.

In Fig. 5, the intersection of the δ–P curve and the $\Delta\delta$–Δf curve is a stable operating point. The operating region II of DFIG is considered in this work. When the wind speed rapidly increases, the output active power of the wind farm also increases, which inevitably leads to frequency deviation, namely, Δfi. Fig. 5 shows that frequency stabilization can be maintained by adjusting the phase angle δ_1. In other words, the phase angle is increased from δ to δ_1. Then, the active power transmitted from WFVSC to GSVSC increases to P_1, so that the input and output active power of the WFVSC can reach a balanced point, which means that the frequency of the large-scale wind farm side can be kept stable. When the active power of the large-scale wind farm decreases, WFVSC maintains the active power balance by reducing its power transmission capacity, which means the frequency of the wind farm side can also be kept stable.

E. Control Scheme of WFVSC and GSVSC

Fig. 6 shows the control scheme of WFVSC and GSVSC in the VSC-HVDC link. In Fig. 6, the LV bus is connected to the large-scale wind farm, which is not given in this figure. Wind farm AC voltage and frequency are controlled by the voltage and frequency controllers, respectively. The phase angle and modulation index are obtained from the frequency and voltage controllers, respectively. A traditional control strategy is used for WFVSC to ensure power transmission from the large-scale wind farm to the load center via the VSC-HVDC link [27], and the DC voltage is set to a constant value and kept stable to guarantee the power balance between WFVSC and GSVSC. Moreover, the reference reactive power is set to 0 so that the power factor can reach 1.0. The merit of this control strategy is that it can support the reactive power when disturbance occurs in the main grid.

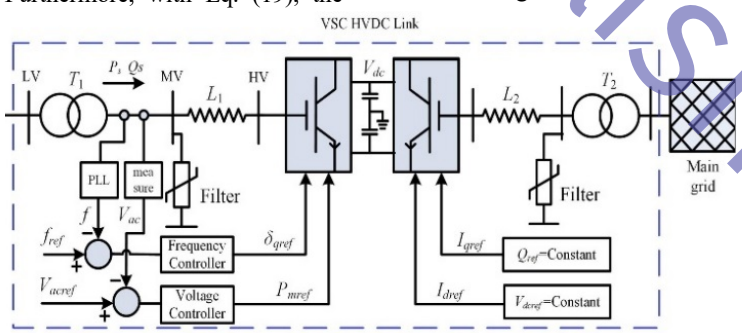

Fig. 6. Control scheme of WFVSC and GSVSC.

III. Parameter Optimization for the Frequency Controller

Eqs. (16) and (20) indicate that the relationship between AC voltage and the modulation index is linear, whereas the relationship between frequency and the phase angle is nearly linear. Therefore, the controller and converter in Fig. 2 can be replaced by two proportional controllers, in which reference frequency f_{ref} is 1.0 p.u and becomes 1/s after Laplace transform. Fig. 7 shows the frequency control structure in the complex frequency domain. The control parameter of the controller is K, and the adjustment parameter of the controller

is K_f. According to Fig. 7, the frequency response function can be obtained as

$$f(s) = KK_f \frac{s + \frac{1}{\tau}}{s(s + \frac{KK_f + 1}{\tau})}. \quad (21)$$

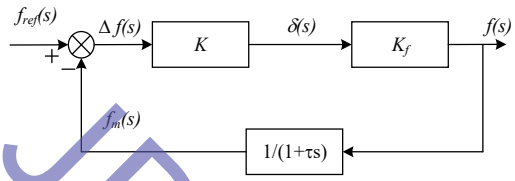

Fig. 7. Frequency control structure in the complex frequency domain.

The parameters of DFIG and the VSC-HVDC link are given in the Appendix. According to these parameters and Eq. (20), we can further obtain K_d=1127.89 and K_f=240.9. We select the best control parameter combination of stable time and overshoot value. Therefore, in terms of $f(s)$ and as shown in Eq. (21), we can obtain the stable time and overshoot value. Fig. 8 shows the frequency response curve in a closed-loop control system by adjusting the parameter K. K is set to have different values, i.e., K=0.1, K=0.5, K=0.7, and K=0.9.

TABLE I
FREQUENCY STABILITY TIME AND OVERSHOOT VALUE DISTRIBUTION AT DIFFERENT K VALUES

K	T_s/s	σ/%	K	T_s/s	σ/%
0.1	0.1000	19.50	0.6	0.0665	12.70
0.2	0.0787	16.70	0.7	0.0753	10.50
0.3	0.0640	15.10	0.8	0.0777	8.93
0.4	0.0702	14.20	0.9	0.0958	9.33
0.5	0.0642	13.40	1.0	0.0782	7.55

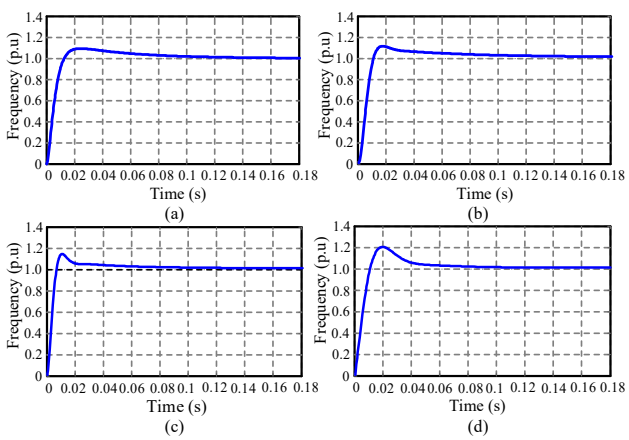

Fig. 8. Frequency response of the designed controller with different control gains. (a) K = 0.9, (b) K = 0.7, (c) K = 0.5, and (d) K = 0.1.

From Fig. 8, we can also calculate the stability time T_s and the overshoot of step response σ at different K values, as shown in Table I. Table I shows detailed frequency stable time T_s and its overshoot value σ when K is set to different values. Stability time and overshoot achieve improved balance when K=0.5. Therefore, K=0.5 is selected as the parameter of the frequency controller in this work. Similarly, in order to select the parameter of the AC voltage controller, we use the same parameter selection method. The parameter of the controller is set to 0.08. Fig. 8 also indicates that when K=0.5, the system frequency response is better than the others and is consistent with the results in Table I.

IV. CASE STUDY

To validate the theoretical analysis and verify the performance of the proposed frequency stabilization and voltage control method, we establish a transient simulation model of a large-scale wind farm based on the VSC-HVDC link, as shown in Figs. 1 and 6. The simulation is carried out by using the DIgSILENT/PowerFactory software. The control strategy of DFIG adopts traditional control. The rotor-side converter of DFIG controls the reactive power and the machine speed, and another converter of DFIG controls the DC-side and AC voltages. WFVSC adopts constant AC voltage control and constant phase angle control (V_{ac}-*phi*) to keep the AC voltage and frequency of the large-scale wind farm stable. GSVSC adopts constant DC voltage control and constant reactive power control (V_{dc}-Q) to keep the DC voltage stable and ensure that the power factor of the main grid reaches unity as soon as possible. Two typical cases, namely, variation of wind speed and single-phase grounding fault, are considered.

A. Case 1: Variation of Wind Speed

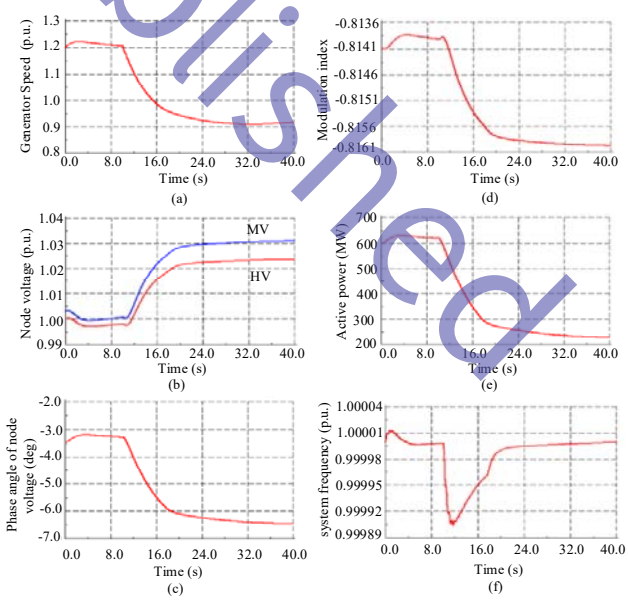

Fig. 9. Dynamic response of the large-scale wind power integrated system under wind speed variation. (a) Generator speed. (b) Node

voltage. (c) Phase angle of node voltage. (d) Modulation index. (e) Active power. (f) System frequency.

In this situation, wind speed is varied within 12 m/s. Fig. 9 shows the dynamic response of the large-scale wind power integrated system via the VSC-HVDC link. The wind speed decreases from 12 m/s to 9 m/s at t=10 s, and the active power of the large-scale wind farm is reduced, which may lead to frequency fluctuation. When the active power decreases suddenly, the frequency controller adjusts the phase angle of WFVSC. Hence, less active power is transferred from the large-scale wind farm to the VSC-HVDC link. Thus, the active power balance between the large-scale wind farm and the VSC-HVDC link is reached, which means the frequency can be kept stable effectively. Under frequency control, the frequency fluctuation of the large-scale wind farm side is 0.006 Hz when the active power of the large-scale wind farm decreases suddenly at t=10 s. Frequency of the large-scale wind farm is recovered at 50 Hz. The relationship between the phase angle of the MV-side's voltage (see Fig. 6) and the PWM modulation index of WFVSC is consistent with Eq. (16) when the DC voltage of the VSC-HVDC link remains constant.

The two wind farms that are integrated into the main grid via the VSC-HVDC link are also studied. One wind farm is composed of 100 DFIGs, and the other wind farm is composed of 200 DFIGs. The initial wind speed of each wind farm is 12 m/s, but the wind speeds of the former and latter wind farms decrease to 2 m/s at t=10 s and 3 m/s at t=25 s. Fig. 10 shows the simulation results of the two large-scale wind farms that are connected to the grid via the VSC-HVDC link. Although the wind speed in the different wind farms fluctuates seriously, the system frequency remains stable, and the frequency fluctuation is merely 0.002 Hz. This result validates the capability of the proposed frequency stabilization control method to keep stabilize the frequency of the large-scale wind farm.

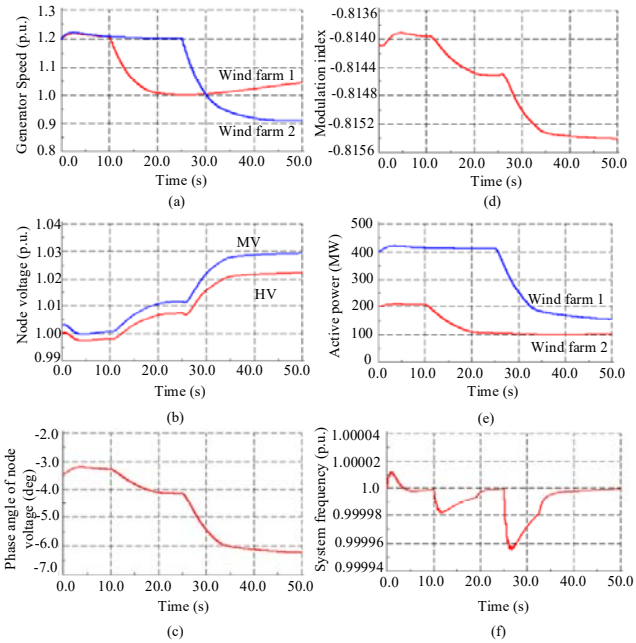

Fig. 10. Dynamic response of the large-scale wind power integrated system consisting of two different wind farms under wind speed variation. (a) Generator speed. (b) Voltage. (c) Phase angle of voltage. (d) Modulation index. (e) Active power. (f) System frequency.

B. Case 2: Single-Phase-to-Ground Fault

In this case, a single-phase-to-ground fault is considered to validate the proposed frequency stabilization method. In node HV, as shown in Fig. 6, a single-phase-to-ground fault occurs at t=2 s. At t=2.5 s, the fault is cleared. In the simulation model, the fault resistance and reactance are set to 0.1 and 0.5 Ω, respectively.

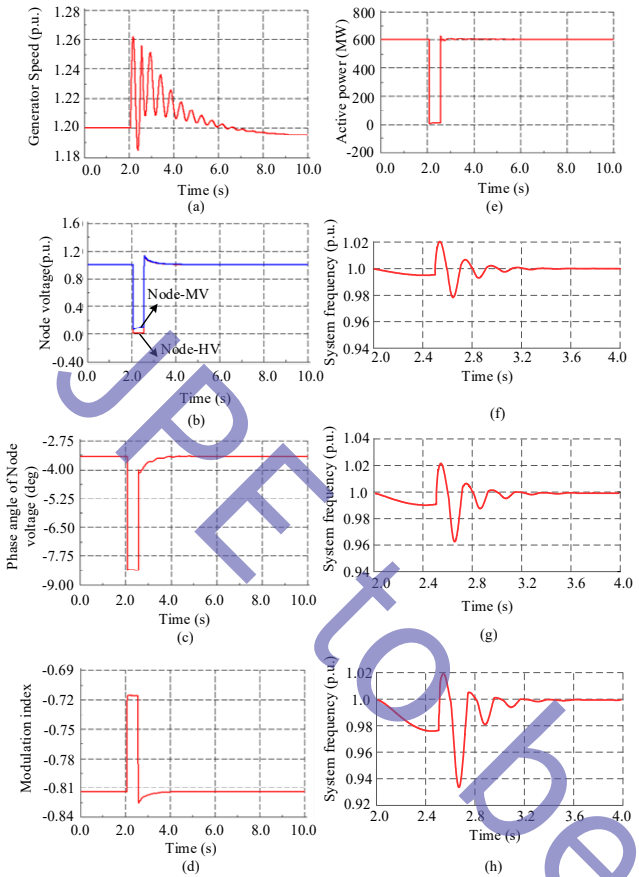

Fig. 11. Dynamic response of the large-scale wind power integrated system under single-phase-to-ground fault. (a) Generator speed. (b) Node voltage. (c) Phase angle of node HV voltage. (d) Modulation index. (e) Active power. (f) K=0.5, (g) K=0.7. (h) K=0.9.

Fig. 11 shows the dynamic response of the large-scale wind power integrated system under the single-phase-to-ground fault. The VSC-HVDC link delivers minimal active power from large-scale wind farm, and the voltage of node HV drops to 0 when the single-phase-to-ground fault occurs. However, the proposed controllers can adjust the PWM modulation index and phase angle to maintain the active power balance between the wind farm side and the VSC-HVDC link. Moreover, the frequency of the large-scale wind farm decreases from 1 p.u to 0.98 p.u, and the frequency recovers to 1 p.u after the fault is cleared. Meanwhile, the voltage of the wind farm also recovers to a normal value. Therefore, the proposed controller has a quick recovery capability that can make the system recover to a stable operating condition after the disturbance is cleared. In comparison with the system frequency response under different K values, as shown in Figs. 11(d), 11(f), and 11(h), when K=0.5, the frequency control can obtains the best dynamic performance during the process of fault, which validates the effectivity of the parameter optimization method presented in Section III.

V. Conclusion

A frequency stabilization control method is developed to improve the stability of a large-scale wind power integrated system based on the VSC-HVDC link. First, the topology of the grid integration of a large-scale wind farm via the VSC-HVDC link is provided, and simple control strategies of DFIG, WFVSC, and GSVSC are described. Second, a mathematical model of the relationship between the phase angle of WFVSC and the frequency of the wind farm is established. The control principle of the large-scale wind power integrated system is revealed theoretically according to the mathematical model. Third, frequency and AC voltage controllers are proposed, and the controller structure is established by deriving the open-loop transfer function. Fourth, an optimization method for selecting the parameters of the frequency controller is presented. Finally, a case study is carried out by using the DIgSILENT/PowerFactory software. The results show that the proposed control method and the optimized controller demonstrate good performance in frequency stabilization. When the wind speed changes, the fluctuation in system frequency is relatively small. Even when the wind farms present changes in a wide range or when the system is disturbed by a phase-to-ground fault, the system frequency can still be kept stable. Moreover, grid integration of the large-scale wind farm via the VSC-HVDC link presents good performance in fault recovery, which indicates that the proposed method can also improve the fault ride through the capability of the large-scale wind farms. The proposed control strategy can also be applied to other fields and types of renewable energies integrated into power systems via VSC-HVDC or multi-terminal VSC-HVDC technology.

Appendix

TABLE II
Parameters of the VSC-HVDC Link

Parameters	Value
Rated apparent power	1216 MVA
Rated DC voltage	640 kV
Rated AC voltage	416 kV
Rated frequency	50 Hz
Transformer rated capacity	1290 MVA
Transformer ratio	400 kV/ 416 kV
Series inductance	75 mH
DC cable length	100 km
DC capacitance	47.029 uF
Modulation index	P_m=1.2
Time constant	τ=0.05
Phase angle	4.7

Acknowledgment

This work was supported in part by the National Natural Science Foundation of China (NSFC) under Grant 61673398, the Research and Innovation Foundation for Graduate Students of Hunan Province under Grant CX2017B105, the

Hunan Provincial Key Laboratory of Wind Generator and Its Control under Grant 2016FLFDYB01, and the Hunan Science and Technology Project under Grant 2016GK2018.

REFERENCES

[1] C. L. Nguyen and H. H. Lee, "Power management approach to minimize battery capacity in wind energy conversion system," *IEEE Trans. Ind. Appl.*, Vol. 53, No. 5, pp. 4843-4854, Sep/Oct. 2017.

[2] Y. Phulpin, "Communication-free inertia and frequency control for wind generators connected by an HVDC-Link," *IEEE Trans. Power Syst.*, Vol. 27, No. 2, pp. 1136-1137, May 2012.

[3] Global Wind Energy Council, Global wind report. Annual market update 2016.

[4] B. Silva, C. L. Moreira, L. Seca, Y. Phulpin, and J. A. P. Lopes, "Provision of inertial and primary frequency control services using offshore multi-terminal HVDC networks," *IEEE Trans. Sustain. Energy*, Vol. 3, No. 4, pp. 800-808, Oct. 2012.

[5] Z. Miao, L. Fan, D. Osborn, and S. Yuvarajan, "Wind farms with HVDC delivery in inertial response and primary frequency control," *IEEE Trans. Energy Convers.*, Vol. 25, No. 4, pp. 1171-1178, Dec. 2010.

[6] H. Zhao, Q. Wu, J. Wang, Z. Liu, M. Shahidehpour, and Y. Xue, "Combined active and reactive power control of wind farms based on model predictive control," *IEEE Trans. Energy Convers.*, Vol. 32, No. 3, pp. 1177-1187, Sep. 2017.

[7] S. Liu, X. Wang, L. Ning, B. Wang, M. Lu, and C. Shao, "Integrating offshore wind power via fractional frequency transmission system," *IEEE Trans. Power Del.*, Vol. 32, No. 3, pp. 1253-1261, Jun. 2017.

[8] A. Colmenar-Santos, J. Perera-Perez, D. Borge-Diez, and C. dePalacio-Rodríguez, "Offshore wind energy: A review of the current status, challenges, and future development in Spain," *Renew. Sustain. Energy Rev.*, Vol. 64, pp. 1-18, Oct. 2016.

[9] B. Gustavsen, and O. Mo, "Variable transmission voltage for loss minimization in long offshore wind farm AC export cables," *IEEE Trans. Power Del.*, Vol. 32, No. 3, pp. 1422-1431, Jun. 2017.

[10] J. Arrillaga, *High Voltage Direct Current Transimission. London: The Institution of Engineering and Technology*, 1998.

[11] L. Wang and M. S. N. Thi, "Comparative stability analysis of offshore wind and marine-current farms feeding into a power grid using HVDC links and HVAC line," *IEEE Trans. Power Del.*, Vol. 28, No. 4, pp. 2162-2171, Oct. 2013.

[12] S. Nouri, E. Babaei, and S. H. Hosseini, "A new AC/DC converter for the interconnections between wind farms and HVDC transmission lines," *J. Power Electron.*, Vol. 14, No. 3, pp. 592-597, May 2014.

[13] Y. Li, F. Liu, L. Luo, C. Rehtanz, and Y. Cao, "Enhancement of commutation reliability of an HVDC inverter by means of an inductive filtering method," *IEEE Trans. Power Electron.*, Vol. 28, No. 11, pp. 4917-4929, Nov. 2012.

[14] C. Guo, C. Zhao, M. Peng, and W. Liu, "Investigation of a hybrid HVDC system with DC fault ride-through and commutation failure mitigation capability," *J. Power Electron.*, Vol. 15, No. 5, pp. 1367-1379, Sep. 2015.

[15] A. A. V. Meer, M. Gibescu, M. A. M. M. V. Meijden, W. Kling, and J. A. Ferreira, "Advanced hybrid transient stability and EMT simulation for VSC-HVDC systems," *IEEE Trans. Ind. Electron.*, Vol. 30, No. 3, pp. 1057-1066, Jun. 2015.

[16] R. Blasco-Gimenez, N. Aparicio, S. Ano-Villalba, and S. Bernal-Perez, "LCC-HVDC connection of offshore wind farms with reduced filter banks," *IEEE Trans. Ind. Electron.*, Vol. 60, No. 6, pp. 2372-2380, Jun. 2013.

[17] Y. Xue and X. Zhang, "Reactive power and AC voltage control of LCC HVDC system with controllable capacitors," *IEEE Trans. Power Syst.*, Vol. 32, No. 1, Jan. 2017.

[18] S. Bozhko, G. Asher, R. Li, J. Clare, and L. Yao, "Large offshore DFIG-based wind farm with line-commutated HVDC connection to the main grid: Engineering studies," *IEEE Trans. Energy Convers.*, Vol. 23, No. 1, pp. 119-127, Mar. 2008.

[19] R. E. Torres-Olguin, M. Molinas, and T. Undeland, "Offshore wind farm grid integration by technology with LCC-based HVDC transmission," *IEEE Trans. Sustain. Energy*, Vol. 3, No. 4, pp. 899-904, Oct. 2012.

[20] A. Egea-Àlvarez, M. Aragüés-Peñalba, and E. Prieto-Araujo, "Power reduction coordinated scheme for wind power plants connected with VSC-HVDC," *Renew. Energy*, Vol. 107, pp. 1-13, Jul. 2017.

[21] P. Mitra, L. Zhang, and L. Harnefors, "Offshore wind integration to a weak grid by VSC-HVDC links using power synchronization control: A case study," *IEEE Trans. Power Del.*, Vol. 29, No. 1, pp. 453-461, Feb. 2014.

[22] D. Xiang, L. Ran, J. R. Bumby, P. J. Tavner, and S. Yang, "Coordinated control of an HVDC link and doubly fed induction generator in a large offshore wind farm," *IEEE Trans. Power Del.*, Vol. 21, No. 1, pp. 463-471, Jan. 2016.

[23] R. Li, S. Bozhko, and G. Asher, "Frequency control design for offshore wind farm grid with LCC-HVDC link connection," *IEEE Trans. Power Electron.*, Vol. 23, No. 3, May. 2008.

[24] R. Li, S. V. Bozhko, G. M. Asher, L. Yao, and L. Ran, "Offshore grid frequency control design for line-commuted converters high-voltage direct-current link connected wind farms," *IET Renew. Power Gener.*, Vol. 1, No. 4, pp. 211-219, Dec. 2007.

[25] H. Liu and Z. Chen, "Contribution of VSC-HVDC to frequency regulation of power system with offshore wind generation," *IEEE Trans. Energy Convers.*, Vol. 30, No. 3, pp. 918-926, Sep. 2015.

[26] Y. Li, Z. Xu, J. Østergaard, and D. J. Hill, "Coordinated control strategy for offshore wind farm integration via VSC-HVDC for system frequency support," *IEEE Trans. Energy Convers.*, Vol. 32, No. 3, pp. 843-856, Sep. 2017.

[27] J. F. M. Padrón, and A. E. F. Lorenzo, "Calculating steady-state operating conditions for doubly-fed induction generator wind turbines," *IEEE Trans. Power Syst.*, Vol. 25, No. 2, pp. 922-928, May, 2010.

[28] C. Guo and C. Zhao, "Supply of an entirely passive AC network through a doubly-infeed HVDC system," *IEEE Trans. Power Electron.*, Vol. 24, No. 11, pp. 2835-2841, Nov. 2010.

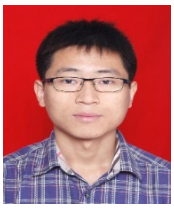

Yanjian Peng was born in Shandong, China, in 1988. He received his B.Sc. degree in electrical engineering and automation from University of Jinan (UJN), Jinan, China, in 2011. He is working toward his Ph.D. degree in the College of Electrical and Information Engineering, Hunan University, Changsha, China. His current research interests include grid integration of renewable energy and analysis and control of power quality.

Yong Li was born in Henan, China, in 1982. He received his B.Sc. and Ph.D. degrees in 2004 and 2011, respectively, from the College of Electrical and Information Engineering, Hunan University (HNU), Changsha, China. Since 2009, he has been working as a research associate at the Institute of Energy Systems, Energy Efficiency, and Energy Economics, TU Dortmund University, Germany, where he received his second Ph.D. degree in June 2012. He is a full-time professor of electrical engineering in HNU. His current research interests include AC/DC energy conversion systems, analysis and control of power quality, and HVDC and FACTS technologies.

Fang Liu was born in Jiangxi, China, in 1982. She received her B.S. degree from the College of Electrical and Information Engineering, Zhengzhou University of Light Industry, Zhengzhou, China, in 2005 and her M.S. degree from the School of Information Science and Engineering, Central South University (CSU), Changsha, China, in 2007. She obtained her Ph.D. degree from in Waseda University, Japan, in 2011. She is an associate professor at CSU. Her research interests include power electronics control and robust control of FACTS with wide-area signals.

Zhiwei Xu was born in Hunan, China, in 1978. He received his M.S. and Ph.D. degrees in 2006 and 2014, respectively, from the College of Electrical and Information Engineering, Hunan University (HNU), Changsha, China. He is currently an associate professor of mechanical engineering at Hunan Institute of Engineering, Xiangtan, China. His current research interests include wind power generation and its control, power electronic transformer systems, and special motors and control.

Yijia Cao was born in Hunan, China, in 1969. He graduated from Xi'an Jiaotong University, Xi'an, China, in 1988 and received his M.Sc. degree from Huazhong University of Science and Technology (HUST), Wuhan, China, in 1991. He obtained his Ph.D. degree from HUST in 1994. He is a full-time professor and the vice president of Hunan University, Changsha, China. His research interests include power system stability control and application of intelligent systems in power systems.